Ultrathin regime growth of atomically flat multiferroic gallium ferrite films with perpendicular magnetic anisotropy

Suvidyakumar Homkar,[1] Daniele Preziosi,[1] Xavier Devaux,[2] Corinne Bouillet,[1] Johanna Nordlander,[3] Morgan Trassin,[3] François Roulland,[1] Christophe Lefèvre,[1] Gilles Versini,[1] Sophie Barre,[1] Cédric Leuvrey,[1] Marc Lenertz,[1] Manfred Fiebig,[3] Geneviève Pourroy,[1] and Nathalie Viart[1]

[1]*IPCMS, UMR Unistra-CNRS 7504, 23 rue du Læss, BP 43, 67034 Strasbourg Cedex 2, France*

[2]*Université de Lorraine, CNRS, IJL, F-54000 Nancy, France*

[3]*Department of Materials, ETH Zurich, Vladimir-Prelog-Weg 4, 8093 Zurich, Switzerland*

(Received 17 October 2019; published 30 December 2019)

Room temperature magnetoelectric multiferroic thin films offer great promises for the spintronics industry. The actual development of devices, however, requires the production of ultrathin atomically smooth films of high crystalline quality in order to increase spin transfer efficiency. Using both high-resolution transmission electron microscopy and atomically resolved electron energy loss spectroscopy, we unveil the complex growth mechanism of a promising candidate, gallium ferrite. This material, with its net room-temperature magnetization of approximately 100 emu/cm^3, is an interesting challenger to the antiferromagnetic bismuth ferrite. We obtained atomically flat gallium ferrite ultrathin films with a thickness control down to one fourth of a unit cell. Films with thicknesses as low as 7 nm are polar and show a perpendicular magnetic anisotropy of 3×10^3 J/m^3 at 300 K, which makes them particularly attractive for spin current transmission in spintronic devices, such as spin Hall effect based heavy-metal / ferrimagnetic oxide heterostructures.

DOI: 10.1103/PhysRevMaterials.3.124416

I. INTRODUCTION

The electronics industry is yearning to benefit from the wide range of sizeable improvements potentially offered by multifunctional oxides. Magnetoelectric multiferroics are among the most promising ones, allowing the manipulation of magnetic properties by an electric field. Despite their scarcity, they inspire a strong research activity with high expectations mainly in the field of low-power spintronics [1–6]. The difficulty to retain and/or shift their magnetoelectric multiferroic properties towards room temperature, especially in the form of thin films [7], makes the growth optimization process of these oxides a necessary step towards their effective implementation. The literature presents various examples where heterostructuring and epitaxial strain have been used to modify the multiferroic properties of high quality bismuth ferrite [8–10] thin films. On the contrary, thin films of room-temperature magnetoelectric multiferroic $Ga_{2-x}Fe_xO_3$ ($0.7 \leqslant x \leqslant 1.4$) (GFO$x$) have not been much studied in that perspective, despite the alternative interesting features this material can bring [11,12]. Bulk GFOx is ferrimagnetic with a net magnetization and a Curie temperature above room temperature for $x > 1.3$ [13]. These properties are retained in thin films and a room temperature magnetization of 100 emu/cm^3 is observed for GFO1.4 thin films [11]. GFO shows a linear magnetoelectric effect of approximately 10^{-11} s/m [13,14] and a spontaneous polarization of about 25 μC/cm^2 [15,16]. It crystallizes in the polar orthorhombic $Pna2_1$ (equivalently $Pc2_1n$) space group, different from the usual perovskite structure adopted by other magnetoelectric compounds, with $a = 0.5086(2)$ nm, $b = 0.8765(2)$ nm, and $c = 0.9422(2)$ nm for $x = 1.4$ [17]. Its structure is based on a double hexagonal compact stacking of oxygens with cations occupying four different sites: a tetrahedral one, Ga1, and three octahedral ones, Ga2, Fe1, and Fe2. The complexity of this structure makes its deposition as thin films with controlled interfaces difficult. Among the few studies in the literature reporting on the growth of thin films of GFOx [11,18–20], none addresses the growth mode nor the possibility to obtain a two-dimensional (2D) growth mode. The need for atomically smooth thin films is, however, a fundamental prerequisite in spintronics to avoid a charge/spin transport degradation across the interface due to electrons scattering [21]. Sharp interfaces are mandatory for observing effects like a spin-orbit torque which is proposed for low-power spintronics devices [22]. A root-mean-square (rms) roughness higher than 1–2 nm ruins the reproducibility of spintronics effects, hindering the desired device integration [23].

In this paper we report on the elucidation of the growth mode of GFO thin films by reflection high energy electron diffraction (RHEED)-assisted pulsed laser deposition (PLD) from the very early stages of the growth. We show that room temperature ferrimagnetic and polar ultrathin films of GFO1.4 with rms roughness of less than a nanometer can be obtained with a control of their thickness down to a fraction of the unit cell. The magnetic anisotropy of the films is tunable *via* the sample thickness. The films already present an electric polarization for a thickness as low as 7 nm. This study lays the ground for realistic use of GFO thin films for spintronics applications.

II. EXPERIMENTAL DETAILS

$Ga_{0.6}Fe_{1.4}O_3$ thin films were deposited on strontium titanate, $SrTiO_3$ (STO) (111) substrates (Furuuchi Chemical Corporation, Japan, with rms roughness lower than 0.15 nm)

using a PLD system having a base pressure of 2×10^{-8} mbar. A polycrystalline target of stoichiometric $Ga_{0.6}Fe_{1.4}O_3$ composition was prepared by the ceramic method [24] and ablated with a 248-nm wavelength KrF excimer laser at a repetition rate of 2 Hz in an oxidizing atmosphere with a O_2 partial pressure of 0.1 mbar. The target-substrate distance was 5.5 cm and the energy density of the laser on the target was $4\,J/cm^2$. The substrate temperature was kept at 900 °C during the growth. *In situ* RHEED was used to monitor the growth of the thin films. The growth was stopped after a number of pulses comprised between 500 and 24 000 to produce GFO samples of different thicknesses. Thickness and structure were studied by x-ray reflectometry and diffraction, respectively, using a Rigaku Smart Lab diffractometer equipped with a rotating anode and a monochromated copper radiation (1.54056 Å). The surface of the films was observed and their rms roughness quantified by atomic force microscopy (AFM) using a Bruker ICON microscope in tapping mode. Energy dispersive x-ray spectroscopy (EDX) coupled to a scanning electron microscopy technique (JEOL 6700 F) was used to check the overall composition of the films. The analysis was performed at 5 keV, ensuring a large surface sensitivity of the EDX signal. Observations of the films in cross sections were performed by high resolution transmission electron microscopy (HR TEM) and high-resolution scanning transmission electron microscopy (HR STEM) using a probe corrected microscope JEOL ARM200F equipped with the Gatan GIF Quantum SE system for electron energy loss spectroscopy (EELS). The lamellae were prepared by focused ion beam (FIB) and rethinned by low voltage (200 V) precision Argon ion milling. The microscope was operated at 80 kV. Multivariate statistical analysis has been used to improve the quality of the STEM-EELS mapping data. We studied the electric polarization state of the films by optical second harmonic generation (SHG). SHG is a nonlinear optical process denoting the emission of light at frequency 2ω from a crystal irradiated with light at frequency ω [25]. This is expressed by the equation $P_i(2\omega) = \varepsilon_0 \sum_{j,k} \chi^{(2)}_{ijk}\ E_j(\omega)E_k(\omega)$, where $E_{j,k}(\omega)$ and $P_i(2\omega)$ are the electric-field components of the incident light and of the nonlinear polarization, respectively, with the latter acting as the source of the SHG wave. The nonlinear susceptibility $\chi^{(2)}_{ijk}$ characterizes the ferroelectric state. The experiments were performed in transmission mode, after polishing the back of the substrate, with a fundamental wavelength of 1200 nm (see Fig. S1 in the Supplemental Material [26]). In our experiments the polarizer [setting $E(\omega)$] and analyzer [selecting component of $E(2\omega)$] are kept parallel to each other and both are rotated simultaneously by 360° to obtain the SHG anisotropy, where 0° and 90° correspond to the vertical and horizontal laboratory axes, respectively. The out-of-plane (OOP) SHG component was extracted from the $\sin^2(x)$-dependence of the SHG intensity on the sample tilt with respect to the incident laser beam, where this angle was varied between −30° and 30°. For probing the GFO films, we used light pulses emitted at 1 kHz from an amplified Ti:sapphire system with an optical parametric amplifier. The light pulses had a photon energy of 1.03 eV, a pulse length of 40 fs, and a pulse energy of 20 μJ. The setup for SHG is described in Ref. [27]. The magnetic properties of the films were studied with a superconducting quantum interference device (SQUID) vibrating sample magnetometer (SQUID VSM MPMS 3, Quantum Design) in both parallel and perpendicular configurations. Hysteresis loops were measured for magnetic fields up to 7 T, at 10, and 300 K.

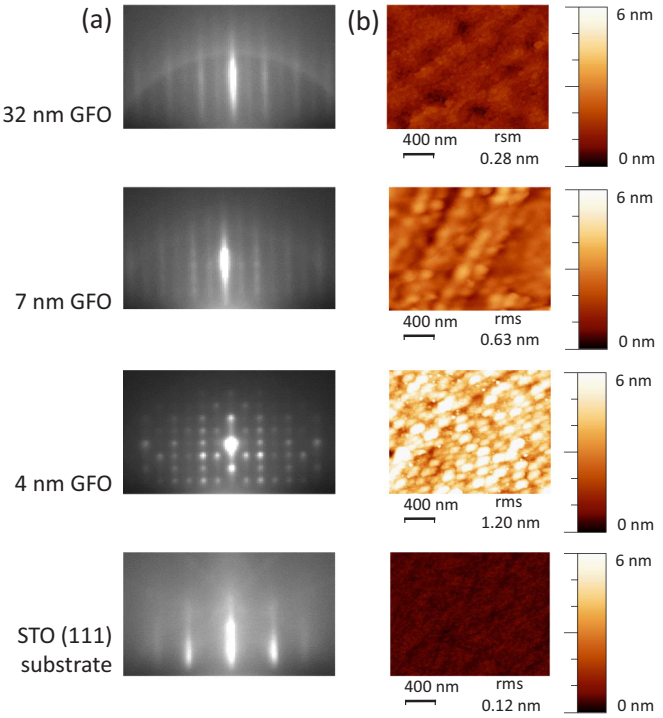

FIG. 1. (a) *In situ* RHEED patterns observed during the growth of GFO1.4 on STO (111). The patterns are taken along the $[\bar{1}2\bar{1}]$ direction of the substrate. The visible lines for the bare substrate correspond to STO $10\bar{1}$ reflections and harmonics. When the growth of GFO starts, some features appear corresponding to GFO 020 reflections and harmonics, the azimuth being along the GFO [100] direction (in the $Pna2_1$ space group). (b) AFM images of the surface of the samples.

III. RESULTS AND DISCUSSION

The *in situ* RHEED monitoring during the GFO1.4 thin-film growth onto STO(111) single crystals rendered a 3D to 2D transition. In order to study this phenomenon, we investigated films of various thicknesses. Figure 1(a) shows some of the RHEED patterns imaged at the end of the deposition. A 3D growth mode is observed at 4 nm as indicated by the dotted RHEED pattern. The RHEED pattern exhibits a transition to a state with a modulated streaky feature at 7 nm, which then becomes fully streaky at 32 nm, indicating a 2D sample surface. The 3D to 2D growth-mode transition as observed via RHEED thus appears for a thickness of approximately 7 nm. The AFM images [Fig. 1(b)] also show an evolution of the surface morphology from randomized islands for 4 nm, through islands aligned in rows, and towards atomically flat films, when islands finally coalesce, in a process very similar to the one reported for the growth of $SrRuO_3$ onto STO (111) [33]. The rms roughness value is around 1 nm at the start of the growth and progressively decreases, with increasing film's

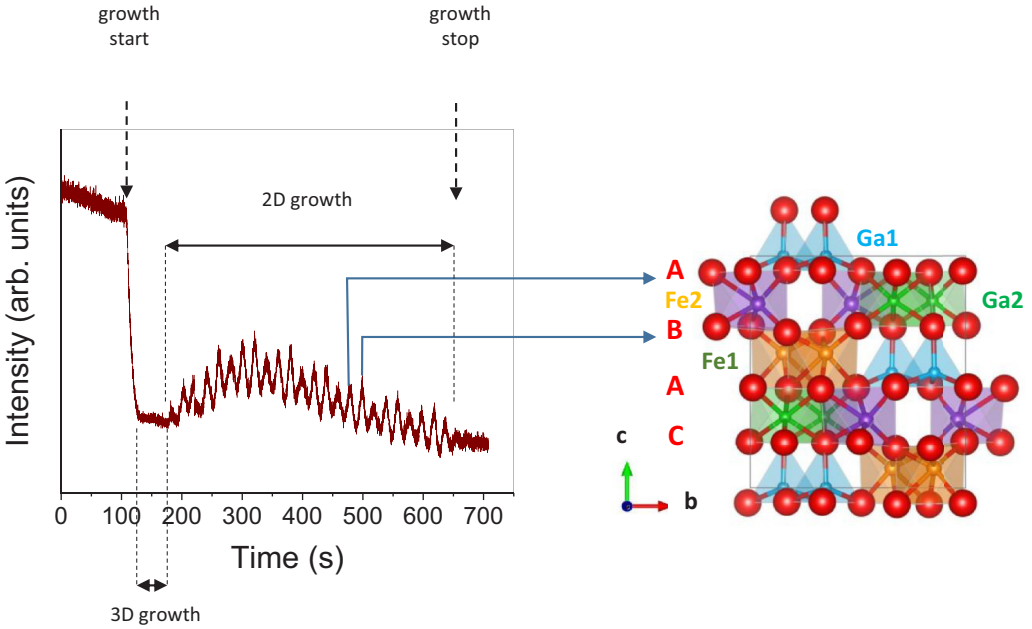

FIG. 2. Fluctuation of the intensity of a spot in the zero-order Laue zone during RHEED monitoring of the 7- nm GFO film growth. Each oscillation corresponds to the deposition of one fourth of a GFO cell, that is, to a layer of transition-metal/oxygen polyhedra.

thicknesses, to values comparable to the rms roughness of the substrate prior to deposition. The growth was also monitored by RHEED from the intensity variation of the spots in the zero-order Laue zone. Figure 2 covers the complete deposition of the 7-nm GFO1.4 film. The overall deposition lasted for 537 s, yielding a deposition rate of 0.0130 nm/s. The 2D growth sets in approximately 108 s after the growth starts, and lasts for 464 s, until the growth is stopped. It shows 24 oscillations. One RHEED oscillation is 19.3 s long. It corresponds to the deposition of 0.25 nm, i.e., about $1/4^{\text{th}}$ of a unit cell. Such a subunit cell growth is rare. It had until now been observed only for the growth of other complex cells, such as those of the spinel [28] or garnet [29] phases of iron oxides.

X-ray diffraction patterns of the deposited films, performed in the θ-2θ mode, are shown in the inset of Fig. 3. They indicate that, for all thicknesses, the GFO thin films are well crystallized, oriented along the $Pna2_1$ [001] axis, without any trace of spurious phase. The observation of Laue oscillations on the zoomed GFO (004) θ-2θ scans confirms high crystallinity and low roughness of the films [Fig. 3]. For the lowest thicknesses, the 00l peaks are shifted towards lower 2θ values, indicating a larger out-of-plane c parameter. The in-plane relationships between the STO (111) surface and the GFO (ab) face are determined from ϕ scans performed on both STO and GFO reflections (see Fig. S2 [26]). GFO may adopt three directions complying with the following epitaxial relationships with STO: [060] GFO (001) // [hkl] STO (111) with [hkl] equal to [$2\bar{2}0$], [$\bar{2}20$] or [$\bar{2}02$]. This is in perfect agreement with the symmetry of the system as shown in Figs. S3 and S4 [26], and as already reported in the literature [19,30,31]. GFO a, b, and c cell parameters could be determined from the combination of θ-2θ scans and reciprocal space mapping of the 206 and 057 reflections (see Fig. S5 [26]). While c decreases with increasing thicknesses (as already observed from the GFO (004) peak in the θ-2θ scans), a and b remain essentially constant (see Fig. S6 [26]). The out-of-plane c parameter reaches the bulk value for thicknesses higher than 64 nm, after a decrease of about 0.2%. The out-of-plane expansion of the c parameter for lower thicknesses is thus not related to any substrate-induced in-plane strain, since it relaxes totally independently from the a and b parameters. The mismatch in this GFO (001) growth on STO

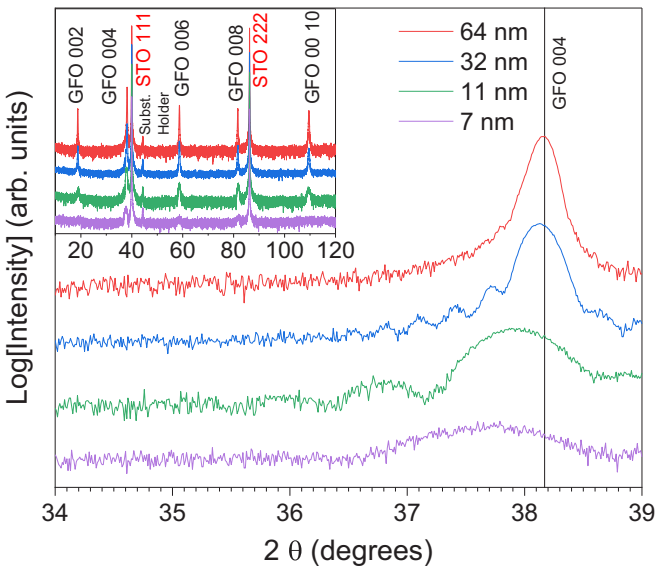

FIG. 3. X-ray diffractograms of the deposited GFO thin films in the θ-2θ mode, with a focus on the GFO 004 peak, the vertical line at $2\theta = 38.17°$ indicates the angle observed for bulk GFO $x = 1.4$ ($c = 0.9422$ nm) [17].

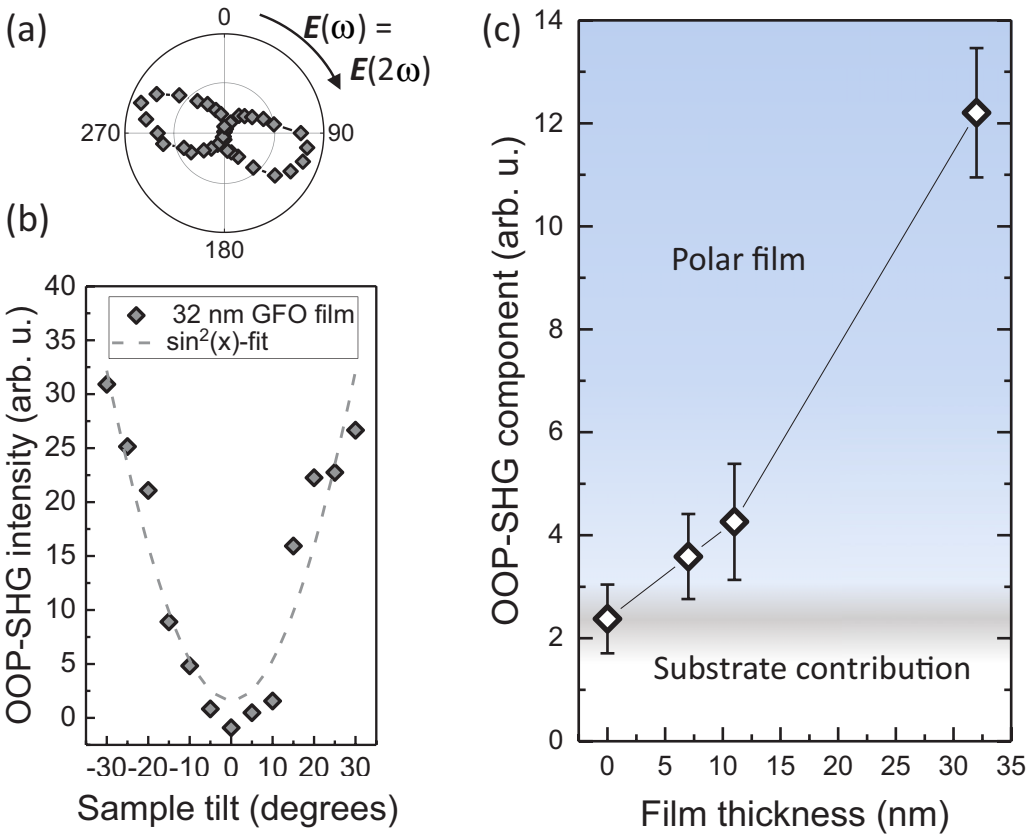

FIG. 4. (a) OOP-SHG anisotropy of the 32 nm GFO film at a 30° tilt. The OOP-SHG is maximized along the projection of the polar axis, which is, along 90°, and exhibits a slight offset from this direction because of interference with the substrate-related SHG contribution. (b) Sample tilt dependence of the OOP SHG-component shown in (a). The $\sin^2(x)$ dependence of the SHG intensity on the tilt angle confirms the OOP orientation of the spontaneous polarization in the material. (c) OOP-SHG at room temperature as function of GFO film thickness. The data point at 0 nm corresponds to measurements on the bare STO(111) substrate. The OOP-SHG component was extracted for each film by a $\sin^2(x)$ fit of SHG tilt-dependence, as shown in (b).

(111) system is large. The distances which have to be considered are (i) along the a_{GFO} direction: $a_{GFO} = 0.5088\,\text{nm} \approx 3d_{STO\,121} = 0.4780\,\text{nm}$ (6.4% compressive strain), and (ii) along the b_{GFO} direction: $d_{GFO\,060} = 0.1465\,\text{nm} \approx d_{STO\,220} = 0.1380\,\text{nm}$ (6.1% compressive strain) (see Figs. S3 and S4 [26]). The relatively high elastic energy introduced by this large strain value accounts for the absence of in-plane strain state in the GFO crystal structure even for the lowest thicknesses. This might also explain the initial 3D mode growth, where totally relaxed GFO islands coalesce while the deposition proceeds to obtain a flat surface. Such a 3D-to-2D metamorphic epitaxial growth [32] mechanism has already been reported for $SrRuO_3$ [33] onto STO and for $\varepsilon - Fe_2O_3$ [34,35], which is isomorphic to GFO. In both cases, the initial 3D growth mode was related to the large lattice mismatch between substrate and thin film.

The electric polarization state of the films was studied by SHG. This contact-free technique is frequently used to probe the breaking of inversion symmetry related to the onset of ferroic order such as spontaneous polarization in bulk crystals and thin films [25]. While the multiferroic properties of bulk GFO have been extensively studied by this technique [36–41], reports on SHG probing of the polar properties of GFO thin films are limited [20,42]. The allowed SHG components related to the polarization in GFO are set by its orthorhombic *mm2* point group with five independent elements. However, in the thin films, due to averaging over the three in-plane 120°-rotated crystallographic variants, the effective point-group symmetry increases to 6*mm*, which holds only three independent components, simplifying the SHG analysis in the thin-film case. By tilting the sample with respect to the incident laser beam, the OOP-SHG component related to the spontaneous polarization along c_{GFO} can be accessed. The SHG dependence on the direction of the incident and detected light polarizations for the 32 nm GFO film at 30° tilt is shown in Fig. 4(a). The double-lobe symmetry mainly along the horizontal direction (along the projection of P_s) is in agreement with the *mm*2 point group averaged over the three crystallographic variants, and with previous bulk [37] and thin film [42] measurements. The offset of the lobes from the horizontal direction is due to a superposition of the STO substrate surface SHG together with the OOP-SHG contributions from the film. The thickness dependence of the GFO electric polarization was studied by performing tilt-dependent SHG measurements [see Fig. 4(b)] on a set of GFO films with varying thicknesses. Reference measurements were carried out on the bare STO substrate. The extracted OOP component of the SHG signal (see Experimental Details) for

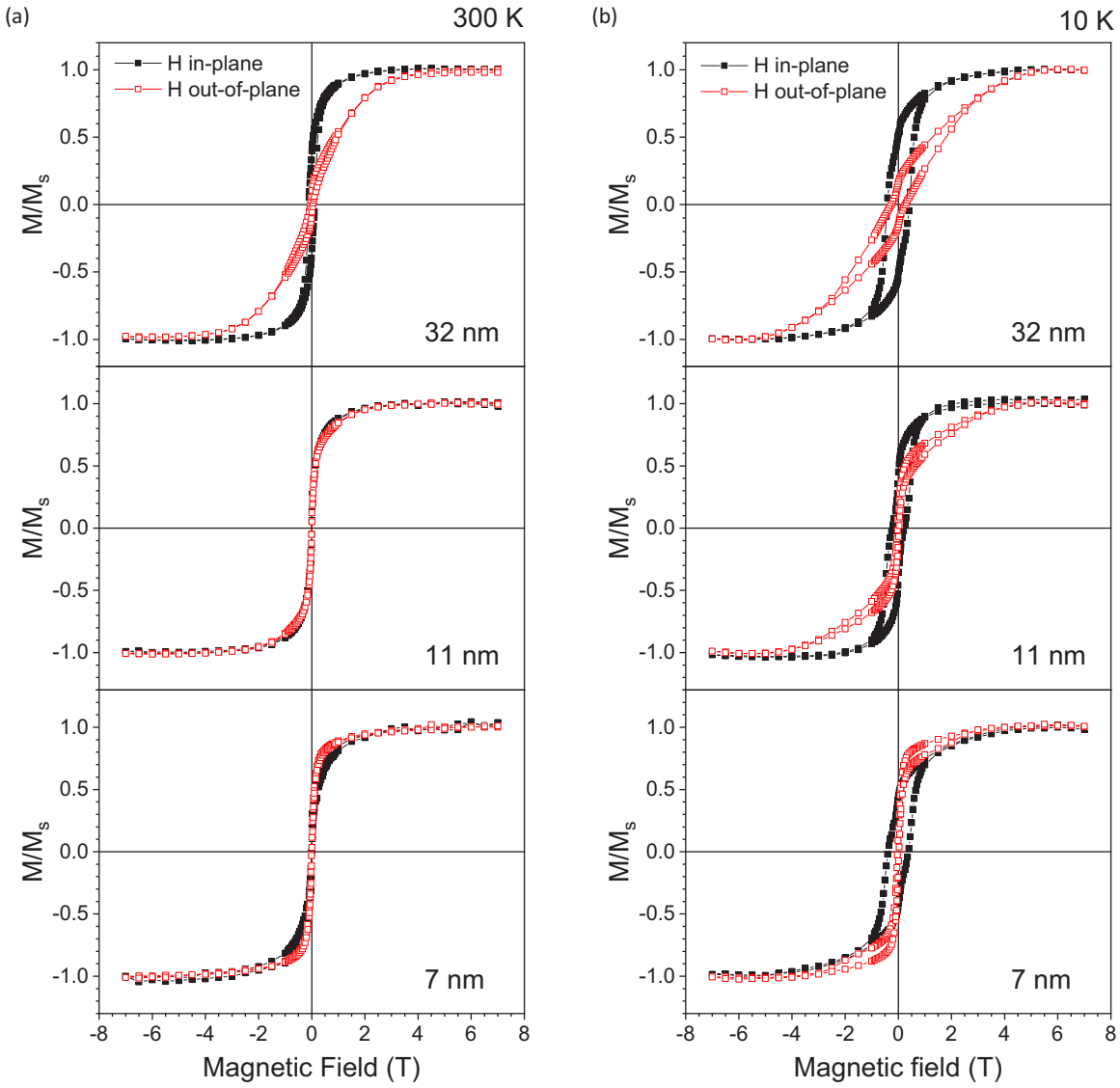

FIG. 5. (a) Room temperature and (b) 10 K magnetic hysteresis loops measured with both in-plane and out-of-plane applied magnetic field for the 32-,11-,and 7-nm-thick samples.

each GFO thickness is plotted in Fig. 4(c). The SHG intensity increases with films thickness. We detect a polarization in our films down to a GFO thickness of 7 nm.

Figure 5 summarizes the magnetic characterization of our GFO thin films series, showing a thickness dependence of the magnetization easy axis. It is worth noting that magnetization lies in-plane for films thicker than 11 nm and is, surprisingly, oriented out-of-plane for the 7-nm-thick sample. This behavior, already observed at room temperature, is clearly confirmed by low temperature measurements [Fig. 5(b)]. Films presenting out-of-plane magnetization are of high interest for spintronic based applications. They indeed address the current challenge to develop high quality sub-10-nm-thick ferrimagnetic insulating films with perpendicular magnetic anisotropy, which are desired for efficient spin current transmission in ferromagnetic/Pt spin Hall effect driven systems [43]. We observed, for samples thicker than 11 nm, the saturation magnetization value of approximately 100 $\mathrm{emu/cm^3}$ already observed for GFO1.4 thick films (100 nm) [11], while the 7-nm-thick GFO sample showed a value of approximately 80 $\mathrm{emu/cm^3}$.

Deeper insight into the structure of the GFO films was obtained with HR STEM. High angle annular dark field (HAADF) images of a cross section of the 32 nm GFO film is presented in Fig. 6. The interface between the STO substrate and the GFO film is well defined and the film shows the cationic pattern expected for GFO in its $Pna2_1$ space-group structure from the beginning of the growth. A zone of darker contrast, indicating a strong evolution of the local chemical composition (lower average atomic number), is clearly visible and delimitates the first five nanometers from the rest of the film. One should note that observations of other areas of the sample reveal a slight dispersion in the position of this delimitation at distances between 2 and 5 nm from the substrate. Mapping the convex or concave shape formed by the four Fe2 and Ga2 sites in a row (*cf.* GFO unit cell in Fig. 2 for the positions of Fe2 and Ga2) allows the determination of the polarization orientation within each unit cell [31].

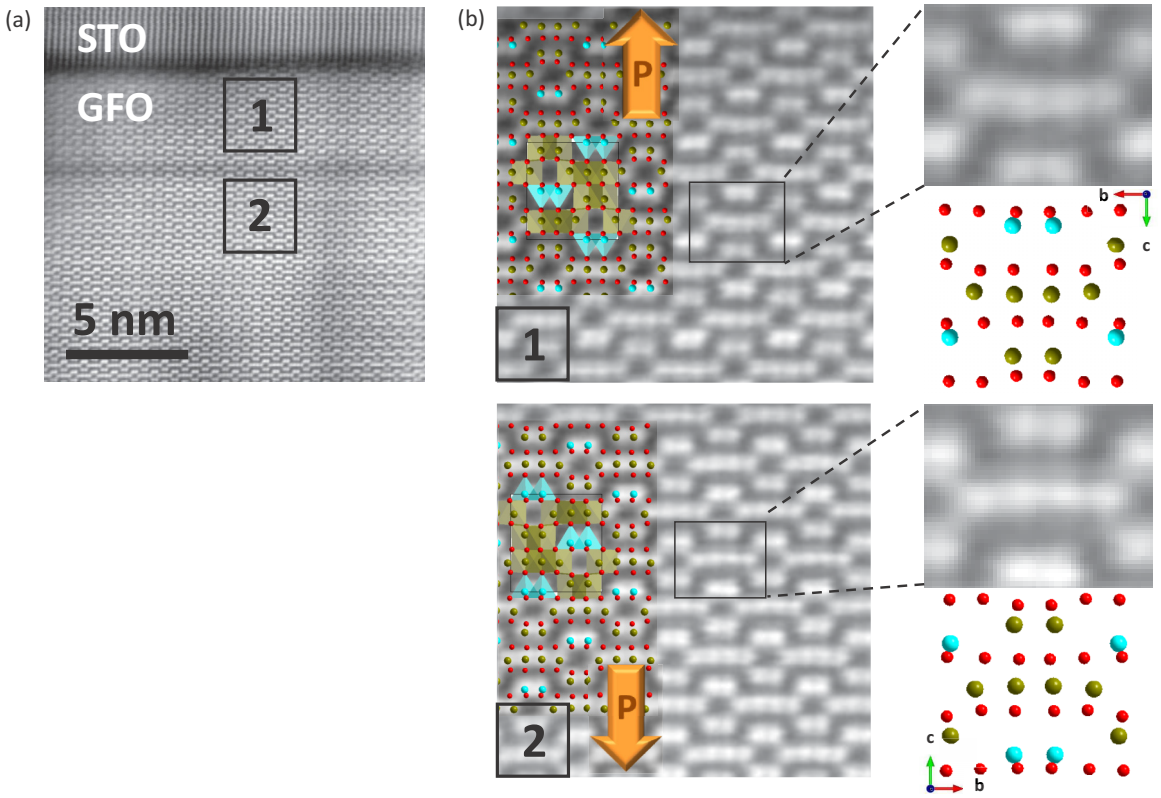

FIG. 6. (a) HAADF HR STEM image of a cross section of the 32 nm GFO film deposited on STO (111) showing that GFO grows in its expected $Pna2_1$ structure from the growth start. A dark line delimitates a first 5-nm-thick GFO layer from the rest of the layer; (b) magnifications of zone 1, showing a polarization pointing towards the substrate, and zone 2, showing a polarization pointing outwards from the substrate. The GFO unit cell and expected atomic pattern for an observation along the [100] zone axis are superimposed on the magnifications; the orientation of the cell is recognizable from the convex or concave feature formed by the four Fe2 and Ga2 octahedral sites in a row (zoomed on the right of the figure).

Interestingly, we observe a polarization reversal as we move away from the film/substrate interface. This corresponds to the first experimental observation of ferroelectric domains in ultrathin GFO films. The domain wall imaged in Fig. 6 corresponds to a nominally charged tail-to-tail configuration. While neutral (normal to the surface) ferroelectric 180° domain formation in the ultrathin regime is expected in absence of charge screening [44–47] for classical systems, the stability of the tail-to-tail domain wall type observed here might be attributed to the highly energetic switching path of GFO. The polarization switching is expected to occur along the $Pna2_1$-to-*Pnna* phase-transition path with an activation energy in the 0.5–1 eV range per formula unit [16,19,48]. This high switching activation energy results in a high coercive field which would therefore stabilize electrostatically unfavorable domain architectures. Similar charge domain walls have only been observed recently in improper ferroelectrics such as $YMnO_3$, in which the domain pattern is set by nonferroelectric primary order parameter [49]. The tail-to-tail polarization configuration, with a domain boundary at about 5 nm from the substrate, may be at the origin of the increased out-of-plane cell parameter, observed for low thicknesses. The tail-to-tail polarization domains are indeed expected to repel each other and therefore lead to an increase of the overall cell parameters. The phenomenon will be less and less appreciable with increasing films thicknesses.

In order to further investigate the origin of the changes in the polarization and magnetization orientations during the early stage of GFO growth, we performed a chemical analysis. Atomically resolved quantitative elemental mappings of the film at the interface with the substrate were obtained by processing the STEM-EELS spectrum [Fig. 7]. Both the Ga and Fe maps in Fig. 7(b) are in perfect agreement with the expected positions of Ga majorly in the Ga1 (tetrahedral) sites, and Fe majorly in the three other (octahedral) sites [see Fig. 7(a)] [31]. The zone of darker contrast, observed at the polarization reversal in Fig. 6(a), is due to the presence of Fe atoms only, on three consecutive cationic layers in this zone in Fig. 7(a). This results in a Ga depleted zone and, Ga being a heavier atom than Fe, to a relative darker contrast. Ti migrates from the STO substrate into the GFO film by an amount of about 6%, over the first 5 nm. The profile of O is very similar to that of Ti. It shows a depletion at the interface and in the very first nanometers of the deposited film (59 at. %, to be compared to the 60% expected for GFO), and then an increasing concentration up to the unit cell orientation reversal (65 at. %, to be compared to the 60% expected for GFO). After the polarization reversal region, the O content restores to the expected value and that of Ti becomes negligible.

When analyzing the profile of the Fe $L_{2,3}$-edges spectra [Fig. 8], one can observe a significant variation between the very first deposited GFO and the rest of the film, in both

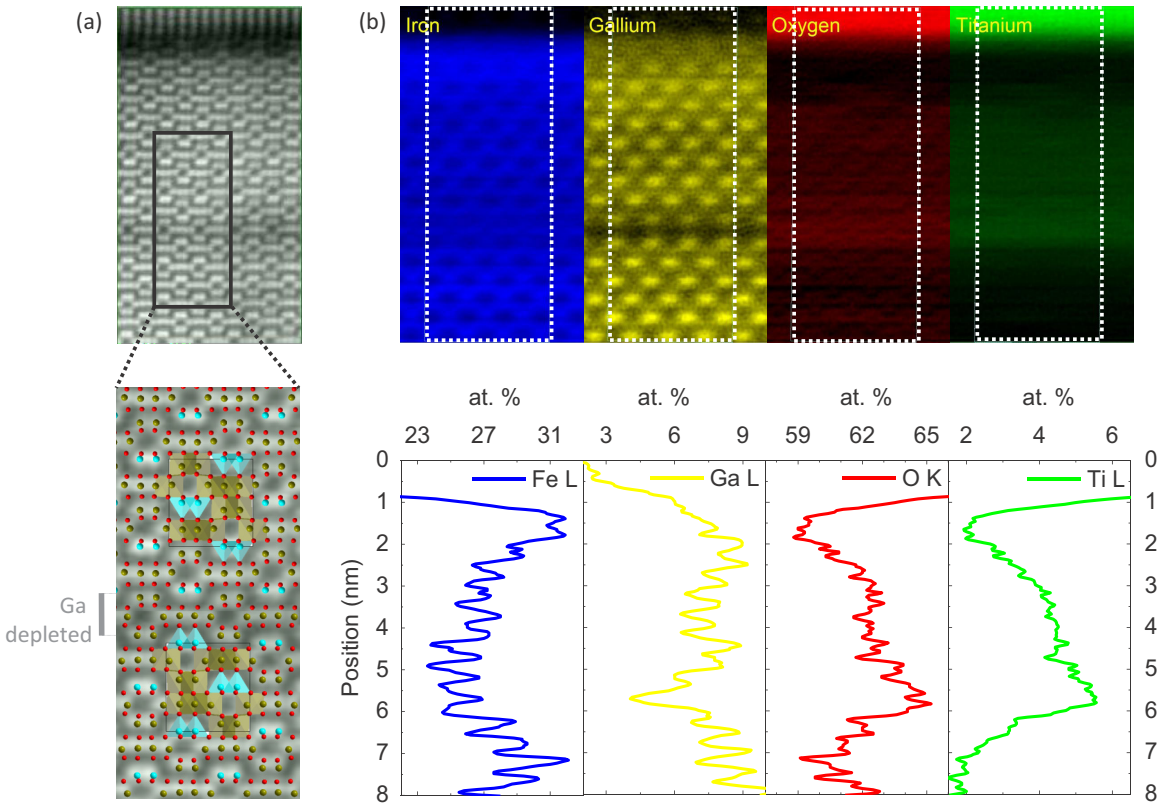

FIG. 7. STEM-EELS analysis of the interface between the STO(111) substrate and the GFO (32 nm) thin film. (a) HAADF survey image and zoom recalling the atomic positions and orientation of the cells on each side of the polarization boundary. (b) Atomically resolved quantitative elemental maps for Fe, Ga, O, and Ti with elemental profiles integrated over the zone of interest (indicated by white dotted rectangles on the maps).

the position of the lines and the intensities ratio at both edges, i.e., $I(L_3)/I(L_2)$. The position of the Fe L_3-edge line is shifted by almost 1 eV towards lower energies in the first two deposited nanometers when compared to the rest of the film. The $I(L_3)/I(L_2)$ ratio (details in Fig. S7 [26]) increases from 3.73 in this area [zone 1 in Fig. 8] to 4.38 for a more inner part of the film [zone 4 in Fig. 8]. Both the Fe excitation edge energy and the $I(L_3)/I(L_2)$ ratio are correlated to the Fe oxidation state [50,51]. Here, they indicate the presence of Fe^{2+} in the early deposited layers of GFO. This is a second possible explanation to account for the increase of the c parameter observed for the very thin films.

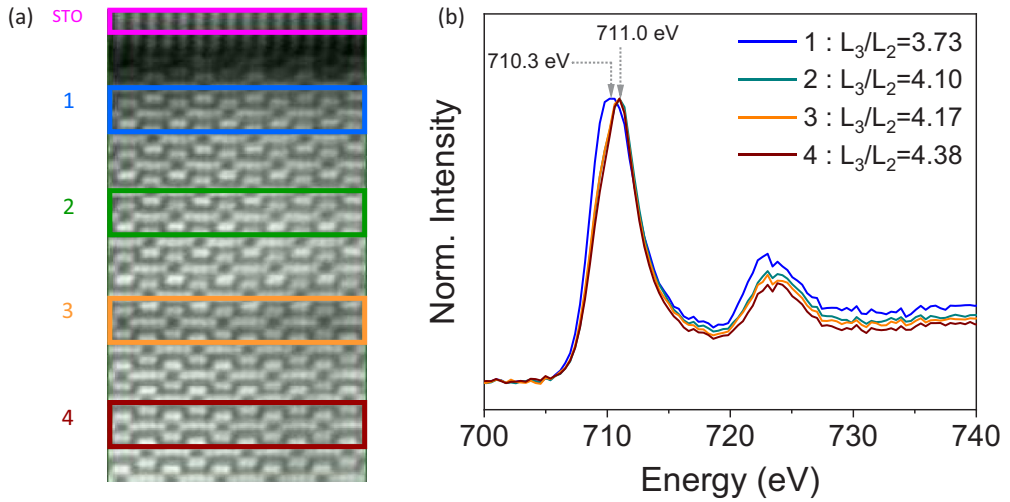

FIG. 8. (a) HAADF HR STEM image of the 32-nm GFO film highlighting four zones at various depths in the films, and (b) the Fe $L_{2,3}$ EELS profiles integrated on these zones.

Indeed, Fe^{2+} has a bigger radius than Fe^{3+}, both in tetrahedral and octahedral sites ($r_{Fe^{2+}_{Oh}} = 0.78$ nm > 0.645 nm $= r_{Fe^{3+}_{Oh}} = 0.78$ nm, and $r_{Fe^{2+}_{Td}} = 0.63$ nm > 0.49 nm $= r_{Fe^{3+}_{Td}}$) [52].

Both HR-TEM and EELS information can be combined to trace back the whole deposition process, from the very first steps of the growth. The following hypotheses may be formulated to describe the mechanism according to which GFO films grow onto STO substrates. At the early stages of the deposition, the Ti atoms of the STO substrate are attracted towards the oxidizing atmosphere at the surface of the sample and diffuse into the forming GFO film, always remaining as close as possible to the free oxygen-rich atmosphere. Such a diffusion phenomenon is promoted by the high temperature at which the sample is maintained during the growth (900 °C). Oxygen-driven cationic mobility has already been observed in other systems [53]. This results in an oxygen-deficient environment for the early grown GFO cells, and therefore to an orientation of their electric polarization towards the substrate. There is indeed a strong relationship between the oxygen concentration and the polarization orientation of polar films [54,55]. The control of the orientation of the polarization of a film through the oxygen partial pressure to which it is submitted has been shown by Wang *et al.* in ultrathin $PbTiO_3$ films [56]. Fe in the first GFO deposited layers is reduced to its +II valence state, as observed by EELS. Ga, which is less prone to reduction, tends to move away from this zone, which is therefore relatively enriched in Fe [see the Fe concentration in the first deposited nanometers in Fig. 7(b)]. The Ti migration from the substrate towards the oxidizing atmosphere of the surface continues as long as the electric conductance of the material allows it. It stops when the GFO film is 5-nm thick and becomes insulating enough to prevent any ionic mobility. The oxygen is then no more cornered by Ti, and the oxygen-rich atmosphere and its correlated negative charges allow a reversal of the polarization [57], which will now point towards the surface until the end of the growth.

Thickness dependent electric polarization orientation had already been observed [58]. The phenomenon was, however, ascribed to already well documented strain-driven effects [57,59,60]. Here the strain-relaxed nature of the GFO films excludes strain-driven effect on the observed polarization reversal within the first 5 nm of the films. Instead, it could have a chemistry-based mechanism and be related to the important ionic migration processes evidenced by HR-TEM and EELS at the substrate-film interface.

The peculiar composition of the first 5 nm of the films, evidenced here by the atomically resolved EELS study, could also account for the modification of the magnetic anisotropy of the GFO films from in- to out-of-plane. Some first principles calculations are currently under way to study the influence of the insertion of Ti in the GFO cell onto its magnetic properties.

IV. CONCLUSION

The pulsed laser deposition of thin films of the magnetoelectric multiferroic compound $Ga_{(2-x)}Fe_xO_3$ ($x = 1.4$) onto STO (111) substrates has been studied from the very early steps of the growth. The growth is initially 3D, because of the mismatch between the substrate and the film but rapidly becomes 2D. A rms roughness as low as 0.16 nm is observed for samples of thicker than 10 nm. The RHEED monitoring resolved one metal-oxygen-polyhedra layer deposition, corresponding to $1/4^{th}$ of a unit cell. All films showed an out-of-plane electric polarization directed towards the substrate for the first few nm and in the opposite direction for the rest of the thickness. Atomically resolved EELS measurements pointed at an ionic migration process driven by electrostatic effects, possibly explaining the magnetic properties for the ultrathin GFO films characterized by an out-of-plane anisotropy. This study therefore lays the ground for the use of multiferroic GFO1.4 thin films in spintronics heterostructures, such as spin-Hall-effect-based heavy-metal / ferrimagnetic oxide heterostructures. The 7-nm-thick sample, with its low rms roughness value and out-of-plane magnetization, is promising to allow efficient spin-current transmission from the heavy-metal (Pt for example) into the ferrimagnetic oxide. A configuration featuring both room temperature out-of-plane net magnetic moment and electric polarization is extremely rare; GFO is only the second oxide system unveiled up to now to display low rms roughness sub-10-nm-thick ferrimagnetic insulating films with out-of-plane magnetization. This opens new perspectives in the field of spin-orbit torque-based spintronics.

ACKNOWLEDGMENTS

This work was funded by the French National Research Agency (ANR) through the ANR MISSION ANR-18-CE-CE24-0008-01 and through the Programme d'Investissement d'Avenir under Contract No. ANR-11-LABX-0058_NIE within the Investissement d'Avenir program ANR-10-IDEX-0002-02. S.H. also acknowledges financial support from ANR through Grant No. ANR-17-EURE-0024 EUR QMat. This research was supported by the EU European Research Council (Advanced Grant No. 694955—INSEETO) and by the Swiss National Science Foundation under Project No. 200021_-178825. The authors wish to thank D. Troadec (IEMN, Lille, France) and A.-M. Blanchenet (UMET, Lille, France) for the preparation of the FIB lamellae, as well as the the XRD, MEB-CRO, and TEM platforms of the IPCMS.

[1] N. A. Spaldin and M. Fiebig, Science **309**, 391 (2005).
[2] X. Chen, A. Hochstrat, P. Borisov, and W. Kleemann, Appl. Phys. Lett. **89**, 202508 (2006).
[3] J. F. Scott, Nat. Mater. **6**, 256 (2007).
[4] Y. H. Chu, L. W. Martin, M. B. Holcomb, M. Gajek, S. J. Han, Q. He, N. Balke, C. H. Yang, D. Lee, W. Hu, Q. Zhan, P. L. Yang, A. Fraile-Rodriguez, A. Scholl, S. X. Wang, and R. Ramesh, Nat. Mater. **7**, 478 (2008).
[5] M. Bibes and A. Barthelemy, Nat. Mater. **7**, 425 (2008).
[6] J. F. Scott, J. Mater. Chem. **22**, 4567 (2012).
[7] N. A. Spaldin and R. Ramesh, Nat. Mater. **18**, 203 (2019).

[8] H. Bea, M. Bibes, S. Petit, J. Kreisel, and A. Barthelemy, Philos. Mag. Lett. **87**, 165 (2007).

[9] M. Bibes, J. E. Villegas, and A. Barthélémy, Adv. Phys. **60**, 5 (2011).

[10] J. Wang, J. B. Neaton, H. Zheng, V. Nagarajan, S. B. Ogale, B. Liu, D. Viehland, V. Vaithyanathan, D. G. Schlom, U. V. Waghmare, N. A. Spaldin, K. M. Rabe, M. Wuttig, and R. Ramesh, Science **299**, 1719 (2003).

[11] M. Trassin, N. Viart, G. Versini, S. Barre, G. Pourroy, J. Lee, W. Jo, K. Dumesnil, C. Dufour, and S. Robert, J. Mater. Chem. **19**, 8876 (2009).

[12] A. Thomasson, S. Cherifi, C. Lefevre, F. Roulland, B. Gautier, D. Albertini, C. Meny, and N. Viart, J. Appl. Phys. **113**, 214101 (2013).

[13] T. Arima, D. Higashiyama, Y. Kaneko, J. P. He, T. Goto, S. Miyasaka, T. Kimura, K. Oikawa, T. Kamiyama, R. Kumai, and Y. Tokura, Phys. Rev. B **70**, 064426 (2004).

[14] G. T. Rado, Phys. Rev. Lett. **13**, 335 (1964).

[15] B. Kundys, F. Roulland, C. Lefevre, C. Meny, A. Thomasson, and N. Viart, J. Eur. Ceram. Soc. **35**, 2277 (2015).

[16] D. Stoeffler, J. Phys.: Condens. Matter **24**, 185502 (2012).

[17] C. Lefevre, F. Roulland, A. Thomasson, C. Meny, F. Porcher, G. Andre, and N. Viart, J. Phys. Chem. C **117**, 14832 (2013).

[18] Z. H. Sun, S. Dai, Y. L. Zhou, L. Z. Cao, and Z. H. Chen, Thin Solid Films **516**, 7433 (2008).

[19] S. Song, H. M. Jang, N.-S. Lee, J. Y. Son, R. Gupta, A. Garg, J. Ratanapreechachai, and J. F. Scott, NPG Asia Mater **8**, e242 (2016).

[20] G. Zhong, Y. Bitla, J. Wang, X. Zhong, F. An, Y.-Y. Chin, Y. Zhang, W. Gao, Y. Zhang, A. Eshghinejad, E. N. Esfahani, Q. Zhu, C. Tan, X. Meng, H.-J. Lin, X. Pan, S. Xie, Y.-H. Chu, and J. Li, Acta Mater. **145**, 488 (2018).

[21] S. Yuasa, T. Nagahama, A. Fukushima, Y. Suzuki, and K. Ando, Nat. Mater. **3**, 868 (2004).

[22] M. Trassin, J. Phys.: Condens. Matter **28**, 033001 (2016).

[23] F. Borgatti, I. Bergenti, F. Bona, V. Dediu, A. Fondacaro, S. Huotari, G. Monaco, D. A. MacLaren, J. N. Chapman, and G. Panaccione, Appl. Phys. Lett. **96**, 043306 (2010).

[24] F. Roulland, C. Lefevre, A. Thomasson, and N. Viart, J. Eur. Ceram. Soc. **33**, 1029 (2013).

[25] J. Nordlander, G. De Luca, N. Strkalj, M. Fiebig, and M. Trassin, Appl. Sci. **8**, 570 (2018).

[26] See Supplemental Material at http://link.aps.org/supplemental/10.1103/PhysRevMaterials.3.124416 for further information on the SHG experimental setup, epitaxial growth of the films, and EELS related calculations.

[27] M. Trassin, G. D. Luca, S. Manz, and M. Fiebig, Adv. Mater. **27**, 4871 (2015).

[28] T. Ojima, T. Tainosho, S. Sharmin, and H. Yanagihara, AIP Adv. **8**, 045106 (2018).

[29] Y. Krockenberger, K.-S. Yun, T. Hatano, S. Arisawa, M. Kawasaki, and Y. Tokura, J. Appl. Phys. **106**, 123911 (2009).

[30] A. Demchenko, Investigation of the Potential Offered by Gallium Iron Oxide Thin Films in Terms of Multiferroicity, Ph.D. thesis, Université de Strasbourg, 2015.

[31] C. Lefevre, A. Demchenko, C. Bouillet, M. Luysberg, X. Devaux, F. Roulland, G. Versini, S. Barre, Y. Wakabayashi, N. Boudet, C. Leuvrey, M. Acosta, C. Meny, E. Martin, S. Grenier, V. Favre-Nicolin, and N. Viart, Small Methods **1**, 1700234 (2017).

[32] C. J. K. Richardson and M. L. Lee, MRS Bull. **41**, 193 (2016).

[33] F. Sánchez, M. V. García-Cuenca, C. Ferrater, M. Varela, G. Herranz, B. Martínez, and J. Fontcuberta, Appl. Phys. Lett. **83**, 902 (2003).

[34] V. Ukleev, S. Suturin, T. Nakajima, T. Arima, T. Saerbeck, T. Hanashima, A. Sitnikova, D. Kirilenko, N. Yakovlev, and N. Sokolov, Sci. Rep. **8**, 8741 (2018).

[35] M. Gich, I. Fina, A. Morelli, F. Sanchez, M. Alexe, J. Gazquez, J. Fontcuberta, and A. Roig, Adv. Mater. **26**, 4645 (2014).

[36] A. M. Kalashnikova, R. V. Pisarev, L. N. Bezmaternykh, V. L. Temerov, A. Kirilyuk, and T. Rasing, JETP Lett. **81**, 452 (2005).

[37] Y. Ogawa, Y. Kaneko, J. P. He, X. Z. Yu, T. Arima, and Y. Tokura, Phys. Rev. Lett. **92**, 047401 (2004).

[38] S. Yamamoto, T. Omi, H. Akai, Y. Kubota, Y. Takahashi, Y. Suzuki, Y. Hirata, K. Yamamoto, R. Yukawa, K. Horiba, H. Yumoto, T. Koyama, H. Ohashi, S. Owada, K. Tono, M. Yabashi, E. Shigemasa, S. Yamamoto, M. Kotsugi, H. Wadati, H. Kumigashira, T. Arima, S. Shin, and I. Matsuda, Phys. Rev. Lett. **120**, 223902 (2018).

[39] M. Matsubara, Y. Kaneko, J.-P. He, H. Okamoto, and Y. Tokura, Phys. Rev. B **79**, 140411 (2009).

[40] K. Eguchi, Y. Tanabe, T. Ogawa, M. Tanaka, Y. Kawabe, and E. Hanamura, J. Opt. Soc. Am. B **22**, 128 (2005).

[41] J.-i. Igarashi and T. Nagao, Phys. Rev. B **82**, 024424 (2010).

[42] D. C. Kundaliya, S. B. Ogale, S. Dhar, K. F. McDonald, E. Knoesel, T. Osedach, S. E. Lofland, S. R. Shinde, and T. Venkatesan, J. Magn. Magn. Mater. **299**, 307 (2006).

[43] A. Quindeau, C. O. Avci, W. Liu, C. Sun, M. Mann, A. S. Tang, M. C. Onbasli, D. Bono, P. M. Voyles, Y. Xu, J. Robinson, G. S. D. Beach, and C. A. Ross, Adv. Electron. Mater. **3**, 1600376 (2017).

[44] D. D. Fong, G. B. Stephenson, S. K. Streiffer, J. A. Eastman, O. Auciello, P. H. Fuoss, and C. Thompson, Science **304**, 1650 (2004).

[45] C. Lichtensteiger, M. Dawber, N. Stucki, J.-M. Triscone, J. Hoffman, J.-B. Yau, C. H. Ahn, L. Despont, and P. Aebi, Appl. Phys. Lett. **90**, 052907 (2007).

[46] M. Dawber, P. Chandra, P. B. Littlewood, and J. F. Scott, J. Phys.: Condens. Matter **15**, L393 (2003).

[47] S. K. Streiffer, J. A. Eastman, D. D. Fong, C. Thompson, A. Munkholm, M. V. Ramana Murty, O. Auciello, G. R. Bai, and G. B. Stephenson, Phys. Rev. Lett. **89**, 067601 (2002).

[48] D. Stoeffler, Thin Solid Films **533**, 93 (2013).

[49] D. Meier, J. Seidel, A. Cano, K. Delaney, Y. Kumagai, M. Mostovoy, N. A. Spaldin, R. Ramesh, and M. Fiebig, Nat. Mater. **11**, 284 (2012).

[50] C. Colliex, M. Tahar, and C. Ortiz, Phys. Rev. B **44**, 11402 (1991).

[51] H. Tan, J. Verbeeck, A. Abakumov, and G. Van Tendeloo, Ultramicroscopy **116**, 24 (2012).

[52] R. Shannon, Acta Crystallogr. Sect. A **32**, 751 (1976).

[53] N. Viart, R. S. Hassan, C. Ulhaq-Bouillet, C. Meny, P. Panissod, J. L. Loison, G. Versini, F. Huber, G. Pourroy, J. Verbeeck, and G. van Tendeloo, Acta. Mater. **54**, 191 (2006).

[54] C. H. Park and D. J. Chadi, Phys. Rev. B **57**, R13961 (1998).

[55] M. J. Highland, T. T. Fister, D. D. Fong, P. H. Fuoss, C. Thompson, J. A. Eastman, S. K. Streiffer, and G. B. Stephenson, Phys. Rev. Lett. **107**, 187602 (2011).

[56] R. V. Wang, D. D. Fong, F. Jiang, M. J. Highland, P. H. Fuoss, C. Thompson, A. M. Kolpak, J. A. Eastman, S. K. Streiffer,

A. M. Rappe, and G. B. Stephenson, Phys. Rev. Lett. **102**, 047601 (2009).

[57] H. W. Jang, S. H. Baek, D. Ortiz, C. M. Folkman, R. R. Das, Y. H. Chu, P. Shafer, J. X. Zhang, S. Choudhury, V. Vaithyanathan, Y. B. Chen, D. A. Felker, M. D. Biegalski, M. S. Rzchowski, X. Q. Pan, D. G. Schlom, L. Q. Chen, R. Ramesh, and C. B. Eom, Phys. Rev. Lett. **101**, 107602 (2008).

[58] X. Yu, L. Wu, B. Zhang, H. Zhou, Y. Dong, X. Wu, R. Kou, P. Yang, J. Chen, C.-J. Sun, Y. Zhu, and G. M. Chow, Phys. Rev. B **100**, 104405 (2019).

[59] T. D. Nguyen, S. Mao, Y.-W. Yeh, P. K. Purohit, and M. C. McAlpine, Adv. Mater. **25**, 946 (2013).

[60] M. Tyunina, O. Pacherova, J. Peräntie, M. Savinov, M. Jelinek, H. Jantunen, and A. Dejneka, Sci Rep **9**, 1 (2019).